Mechanistic Understanding of Stickers Aggregation in Supramolecular Polymers: Quantitative Insights from the Plateau Modulus of Triblock Copolymers

Matthias Nébouy, Julien Morthomas, Claudio Fusco, Laurent Chazeau, Sara Jabbari-Farouji, Guilhem P. Baeza

Mechanistic Understanding of Stickers Aggregation in Supramolecular Polymers: Quantitative Insights from the Plateau Modulus of Triblock Copolymers

Matthias Nébouy[1], Julien Morthomas[1,*], Claudio Fusco[1], Laurent Chazeau[1], Sara Jabbari-Farouji[2] and Guilhem P. Baeza[1,*]

julien.morthomas@insa-lyon.fr

guilhem.baeza@insa-lyon.fr

[1] Univ Lyon, INSA Lyon, UCBL, CNRS, MATEIS, UMR5510, 69621, Villeurbanne, France [1]

[2] Institute of Theoretical Physics (UvA), University of Amsterdam, Science Park 904, 1098, XH, Amsterdam

---

TABLE OF CONTENT

for Table of Contents use only

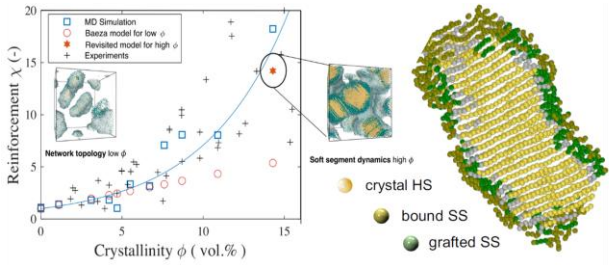

Abstract:

Quantifying the impact of associative groups aggregation on the mechanical properties of dense supramolecular networks remains a challenging problem. To address this question, we carry out coarse-grained molecular dynamics simulations of triblock copolymers consisting of a linear succession of hard-(crystallizable) and soft-(amorphous) segments. This molecular architecture offers the opportunity to increase the volume fraction of crystallites, serving as supramolecular aggregates, in a progressive and controlled fashion, allowing to study its impact on the plateau modulus of the corresponding thermoplastic elastomers. By unifying these simulations with a recent mechanistic model and experimental data, we provide new quantitative insights into the microscopic origin of the mechanical reinforcement. Enhancement of the plateau modulus originates from the network's topology at low crystallites content (< 8 vol.%) while it is dominated by the dynamical slowdown of hardened soft segments, which jointly with the hard phase, form a hybrid percolated network above this threshold.

1. Introduction

Supramolecular polymers consisting of linear macromolecules carrying associative moieties have been thoroughly studied in the last three decades, largely promoted by the attribution of the Nobel Prize in Chemistry to Cram, Lehn and Pedersen in 1987. Since then, major advances in chemistry have led to the development of a wide variety of systems relying on hydrogen bonds, π-π interactions, ionic aggregation and metal-ligand complexation[1–5], often targeting self-healing properties[6]. From a physical point of view, the incorporation of associative groups ("stickers") within the chains enables to decorrelate their segmental and terminal relaxations, respectively driving their glass transition temperature (T_g) and their flow properties. Concretely, active stickers can dramatically slow down the chain diffusion while keeping the glass transition barely unchanged, providing (low T_g) supramolecular networks with an apparent thermoplastic-elastomer-like mechanical behavior. Beyond quantitative decorrelation, many rheological studies have evidenced qualitative differences regarding the temperature dependence of the two processes: while segmental motions obeys William-Landel-Ferry (WLF) dynamics, supramolecular chains diffusion are well-described by Arrhenius profiles, as expected from non-cooperative physical bonds dissociation[7,8].

The description of the rheological behavior of supramolecular polymers was notably addressed by Leibler, Colby and Rubinstein in their seminal paper introducing the Sticky-Rouse and Sticky-Reptation models[9], in which the phenomenology was convincingly captured. By assuming isolated stickers, they provided a well-known expression for the shear plateau modulus (G_N^{supra}), directly derived from the entropic elasticity theory and the affine network model[10] as follows

$$G_N^{supra} \cong cRT\left(\frac{p}{N_s}+\frac{1}{N_e}\right). \quad (1)$$

Here, c is the molar number density of monomers (or Kuhn segments), R is the perfect gas constant, T is the temperature, p is the probability for a sticker to be active that depends on the temperature, N_s is the number of Kuhn segments between successive stickers along a chain and

N_e is the mean number of Kuhn segments between two consequent entanglements. In this paper, the authors focused on the case of $N_s > N_e$, i.e, supramolecular networks formed by chains carrying a low number of stickers, which allowed them to make the hypothesis of non-perturbed chain conformation and absence of phase separation.

However, the development of supramolecular materials has generated a myriad of systems based on dense-supramolecular networks in which the hypothesis of isolated dimer-based stickers (i.e., with a functionality of 4) does not hold true anymore. Among the vast list of examples, a recent study by the group of E. Van Ruymbeke have notably evidenced the massive aggregation of terpyridine-ions moieties in metal-ligand based supramolecular network, resulting in a strong impact on the rheological properties[11]. The same (unexpected) effect was also evidenced on similar (albeit denser) systems by some of us [7]. Interestingly, while the aggregation of stickers might be seen as an undesired effect, researchers have also tried to control it to tune the properties of materials. This philosophy was notably adopted by the group of B. Olsen, where a given number of stickers were progressively concentrated at the chains extremities to generate longer terminal relaxation time[12,13]. In the same vein, the group of R. Colby has developed co-ionomers in which both phase separation and ionic groups aggregation were desired to provide the material with higher mechanical properties[14]. A comprehensive review of the field was published recently by the group of Seiffert[15] pointing the effect of stickers aggregation on various properties of supramolecular polymers. Some of the above-mentioned examples are gathered in Figure 1 to illustrate the shift from isolated stickers towards clusters and super-structures such as ribbon-like assemblies emerging from both associative groups aggregation or hard-segments crystallization.

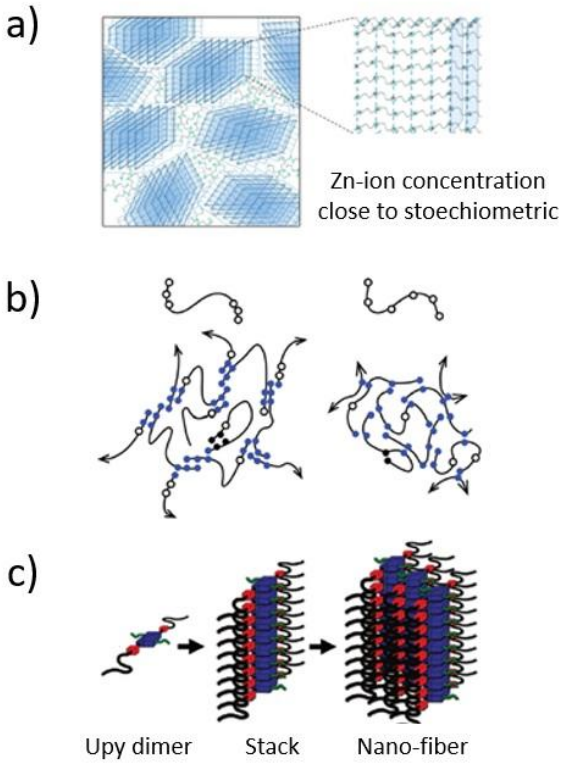

Figure 1: Schematic representation of various supramolecular systems highlighting the presence of stickers aggregates relying on different types of moieties. a) Metal-ligand associative groups gather into tridimensional aggregates, adapted from ref[11]. b) The concentration of histidine stickers at the polymer ends (resulting in a triblock copolymer configuration) enhances their aggregation (left) while the material's structure is homogeneous when stickers are spread regularly along the backbone (right). White and blue dots represent non-active and active stickers respectively, adapted from ref[13]. c) The aggregation of supramolecular UPy moieties results into the formation of ribbon-like crystallites ("nano fibers"), adapted from ref[16].

In spite of an abundant literature and numerous examples of "heterogeneous" supramolecular polymers, it seems however that no general formalism has emerged to link the plateau modulus and the degree of aggregation of the stickers in dense polymer networks (theoretical works are available for some solutions and gels[17,18]). As a matter of fact, Eq. 1 fails to predict the extra-

reinforcement generated by the stickers aggregation and must therefore be adapted, while (ideally) keeping its "universal" character, i.e., being applicable regardless of the chemical nature of the network.

To address this challenge, we propose in this article to consider the case of tri- and multiblock copolymers [(B-A)$_n$-B], both denoted MBCs hereafter, by combining experimental, theoretical and numerical simulations approaches. Actually, simulations concern triblock copolymers only, experimental data come from multiblock copolymers including triblock copolymers, and the analytical modeling is developed for any crystallizable block copolymer with $n \geq 1$. These materials, which are widely used in the industry as thermoplastic elastomers, rely on the phase separation of soft-(A) and hard-(B) segments possibly followed by the crystallization of the latter at low temperature[19,20]. They present the great advantage to cover a wide range of crystallites volume fraction (Φ), representing here a tunable fraction of stickers aggregates. By adjusting the content in hard-segments (HS) within the chain through their density numbers or their length, we therefore have the opportunity to investigate the reinforcement (χ) in a systematic way that we define as

$$\chi = \frac{G_N^{MBC}}{G_N^{SS}}, \tag{2}$$

where G_N^{MBC} and G_N^{SS} are the plateau modulus of the block copolymer and the neat matrix made of soft-segments (SS), respectively. Importantly, the present work supports and enhances our recent mechanistic model[21] that we further use here in parallel to Coarse-Grained Molecular Dynamics (CGMD) simulations to capture a physical understanding of the reinforcement observed in supramolecular polymers in the presence of stickers aggregates.

The article is organized as follows: Section 2 is devoted to a reminder of our analytical model developed for MBCs (2.1) and to the description of technical aspects regarding CGMD simulations (2.2). Section 3 presents simulated mechanical properties of a wide variety of

triblock copolymers and compare these results to previously published experimental data and predictions of our analytical model (3.1). We then focus on the dynamical slowdown of the soft phase in presence of large aggregates to rationalize the reinforcement upturn generally observed at high concentration of supramolecular moieties (3.2).

2. Materials and Methods

2.1 Analytical description

The semi-empirical mechanistic model we use to rationalize the modulus enhancement of multiblock copolymers with increasing the fraction in HS, and corresponding crystallites volume fraction, is detailed in previous works [21,22]. It stems from the entropic elasticity theory and consist of counting the number of additional topological links generated by the HSs association into crystallites. Its ability to describe successfully a wide set of experimental data has been demonstrated in ref[23]. Below, we briefly remind the model ingredients and its prediction for low and high degrees of crystallinity (aggregation).

Low degree of aggregation

In a homogeneous entangled polymer melt, the density of topological nodes (i.e., entanglements) per chain is $1/a^3$, where a is the tube diameter. A sphere of diameter a contains P_e entanglements that however belong to different chains, i.e., do not interact with each other at the length scale relevant for entropic elasticity. In the case of MBCs, we proposed that the association of HSs enables the cooperation of these P_e entanglements by connecting physically the chains they belong to at a lengthscale smaller than a. This approach, illustrated in Figure 2 below, results in a density of topological links per chain being N_{ce}/a^3 , where N_{ce} is the number of HSs included in the volume defined by the intersection of a ribbon-like crystallite and the sphere of diameter a. A naïve mechanical analogy consists of imagining that pulling one of the P_e

strands connected to the crystallite results in solicitating N_{ce} other strands at the tube diameter length scale.

Beyond its link with the crystallites' geometry, N_{ce} further describes the density of the topological network in the sense that it quantifies the number of strands being connected to each other at the tube diameter lengthscale. From this point of view, a wider crystallite is necessarily synonymous of a higher network density, making N_{ce} an indicator of the "chains connectivity". N_{ce} can be easily calculated from the width of the crystallite (W) and its cell parameters in the plane ($\vec{W}, \vec{L}$) orthogonal to the chain axis ($u_L \approx u_W \approx u$), or alternatively, from the distance between the central axes of adjacent crystallites d^* and their volume fraction Φ accessible experimentally,

$$N_{ce} = \frac{Wa}{u_L u_W} = \frac{ad^{*2}}{\mu t u^2}\Phi. \qquad (3)$$

Here, μ is a geometrical parameter that depends on the arrangement of the crystallites (=1, isotropic or 3, aligned)[24], and t is the crystallites thickness, corresponding to the length of the HS. Note that in the case of $W \geq a$, corresponding to the case of a wide lamellar geometry instead of a thin ribbon, we assumed $N_{ce} = \left(\frac{a}{u}\right)^2$.

Taking then the total density of topological links (ν_{tot}) as the weighted sum of contributions coming from the soft and hard phases leads to

$$\nu_{tot} = (1 - \Phi)\nu_{SS} + \Phi N_{ce}\nu_{SS} = \nu_{SS}\,[1 + \Phi(N_{ce} - 1)], \qquad (4)$$

where ν_{SS} is the density of topological links in the soft phase. Assuming that the HSs crystallization has no significant impact on the average conformation nor dynamics of the SSs (which is very likely at low Φ), the reinforcement χ_{low} is then simply the ratio between ν_{tot} and

ν_{SS}, giving a straightforward relationship between the MBC modulus, the volume fraction in crystallites and the inter-crystallites distance

$$\chi_{low} = \frac{\nu_{tot}}{\nu_{SS}} \approx 1 + \frac{ad^{*2}}{\mu t u^2}\Phi^2. \quad (5)$$

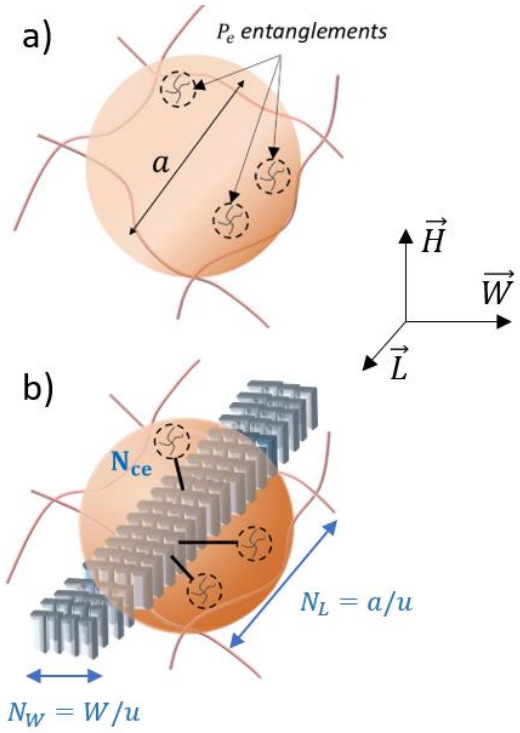

Figure 2: Schematic representation of the local environment of a crystallite and the topological consequences it has on the polymer network. a) Neat soft polymer. b) Multiblock copolymer where N_L, N_H and N_W are the aggregation numbers in the three principal directions $\vec{L}$, $\vec{H}$ and $\vec{W}$ (by construction N_H is always equal to 1), adapted from [21].

In this context, the elastic modulus only stems from entropic considerations assuming that the temperature is far above the glass transition temperature of the SS (close to -60 °C experimentally and 0.46 ε_u/k_B in simulations, see below). For the sake of simplicity, non-associated HSs possibly impacting slightly the dynamics of the amorphous phase [23], are

voluntarily not considered. Note finally that Eq. 5 above, in which all the geometrical parameters appear, can be rewritten in a shorter way, as a function of N_{ce} that is directly accessible in our CGMD simulations.

$$\chi_{low} = 1 + (N_{ce} - 1)\Phi. \quad (6)$$

High degree of aggregation

The hardening of the soft phase caused by the presence of crystallites is defined as

$$H = \frac{G_N^{SS-c}}{G_N^{SS}}, \quad (7)$$

where G_N^{SS} and G_N^{SS-c} are respectively the rubbery modulus of the neat-SS matrix and the one corresponding to its hardened version, i.e., where the confined SSs exhibit dynamical slowing down in presence of crystallites. Following the classic picture of entropic elasticity and assuming that P_e remains constant, one can then rewrite H as a function of the apparent densities of topological links (ν_i) and corresponding tube diameters (a_i) such that

$$H = \frac{\nu^{SS-c}}{\nu^{SS}} = \left(\frac{a}{a_c}\right)^3. \quad (8)$$

Note that while ν^{SS} and a can be measured independently from the neat soft matrix, ν^{SS-c} and a_c are respectively the apparent topological link density and tube diameter characterizing the confined soft phase. Both are used as intermediate (non-measurable) parameters in our model. Then, following the same logic as above (low Φ), where the number of topological links within the hard-phase was expressed as $N_{ce}\nu^{SS}$, we can define the same quantity in MBCs containing a confined soft phase as $N_{ce-c}\nu^{SS-c}$. Assuming that the total density of topological links (ν^{tot-c}) is the volume weighted average of the hardened soft phase (made of SSs) and the hard phase (made of HSs), one obtains

$$\nu^{tot-c} = (1-\Phi)\nu^{SS-c} + \Phi N_{ce-c}\,\nu^{SS-c} = \nu^{SS-c}[1+\Phi(N_{ce-c}-1)]. \qquad (9)$$

Note that our analytical model considers here that the whole soft phase is slowed down (i.e., hardened) in a homogeneous way, i.e., that a unique value of H stands for all the SSs regardless of their position [21]. Refinements of this description are provided below by using CGMD simulations.

Then, because crystallites are expected to widen with increasing Φ [24,25] and that $a_c < a$, it is reasonable to assume that $W > a_c$ (which is confirmed by analyzing quantitatively our simulation boxes), leading to a simplification of Eq. 3 resulting in

$$N_{ce-c} = \left(\frac{a_c}{u}\right)^2, \qquad (10)$$

where a_c depends only on the confined soft phase characteristics and the cell parameters. By isolating a_c in Eq. 8, inserting it into Eq. 10 and replacing the corresponding expression of N_{ce-c} in Eq. 9, we finally obtain the reinforcement in presence of a hardened soft phase

$$\chi_{high} = \frac{\nu^{tot-c}}{\nu^{SS}} \approx H + \Phi\left(\frac{a}{u}\right)^2 H^{1/3}. \qquad (11)$$

Importantly, although we evidence below that the slowing down of the SSs is not homogeneous, i.e., that it depends on their position with respect to the crystallites, we believe that Eq. 11 is applicable as long as hardened SSs and HSs form a percolated network. In this case, the value of H is the one characterizing the most hardened SSs bridges located in-between crystallites while the rest of the SSs, acting in parallel, is considered too soft to play any significant role on the reinforcement.

2.2. Coarse-grained molecular dynamics simulations

Our recent CGMD model[26], where polymer chains consist of “beads” representing a few structural units, is adapted to simulate polybutylene terephthalate / polytetrahydrofuran (PBT/PTHF) MBCs by matching physical characteristics of PBT and PTHF chemical units like chain rigidity and density[27]. In the past, we used this model to study the impact of the molecular weight distribution[28,29] on the crystallization of homopolymers and the effect of the block-length[27] on the crystallization of tri- and penta-block copolymers. This CGMD model[26] is based on two potentials, where energy, length, and time units are given by ε_u σ_u, and τ_u, respectively, with $\tau_u = \sqrt{m_u \sigma_u^2/\varepsilon_u}$ where m_u is the mass unit. Intrachain interactions of bonded beads corresponding to covalent bonds are given by a FENE potential:

$$V_{FENE}(r) = -0.5kR_0^2 ln\left(1 - \left(\frac{r}{R_0}\right)^2\right) + 4\varepsilon\left(\left(\frac{\sigma_F}{r}\right)^{12} - \left(\frac{\sigma_F}{r}\right)^6\right) \qquad (12)$$

with $k = 30\ \varepsilon/\sigma_u^2$, $R_0 = 1.5\ \sigma_u$, $\sigma_F = 1.05\ \sigma_u$ and $\varepsilon = 1\ \varepsilon_u$. All other weak interactions between two beads of different chains or between two nonbonded beads of the same chain are modeled by a Lennard-Jones potential:

$$V_{LJ}(r) = 4\varepsilon\left(\left(\frac{\sigma}{r}\right)^{12} - \left(\frac{\sigma}{r}\right)^6\right) - 4\varepsilon\left(\left(\frac{\sigma}{r_c}\right)^{12} - \left(\frac{\sigma}{r_c}\right)^6\right) \qquad (13)$$

where, $r_c = 2.5\ \sigma_u$ is the cutoff radius and the value of $\sigma = 1.89\ \sigma_u$ has been optimized to make possible the crystallization.

Here, we focus on simulating “triblock" copolymers (HS-SS-HS), containing $N = 2N_{HS} + N_{SS}$ beads per chain, where N_{HS} and N_{SS} are respectively the number of beads per hard and soft segments as illustrated in Figure 3a. Series of molten copolymers named HSX, where $X = N_{HS}$, as well as their neat hard and soft polymer counterpart, respectively named “neat-HS" and “neat-SS", are built by using the radical-like polymerization algorithm[30] at $T = 4\ \varepsilon_u/k_B$. N_{HS} varies from 6 to 20 while N_{SS} is adjusted so that the ratio N/N_e in the MBC melt is kept constant, with

N_e being the number of beads per entangled strand that we evaluate through the Z1 code[31]. The whole list of numerical samples is provided in Table 1 together with their main structural parameters.

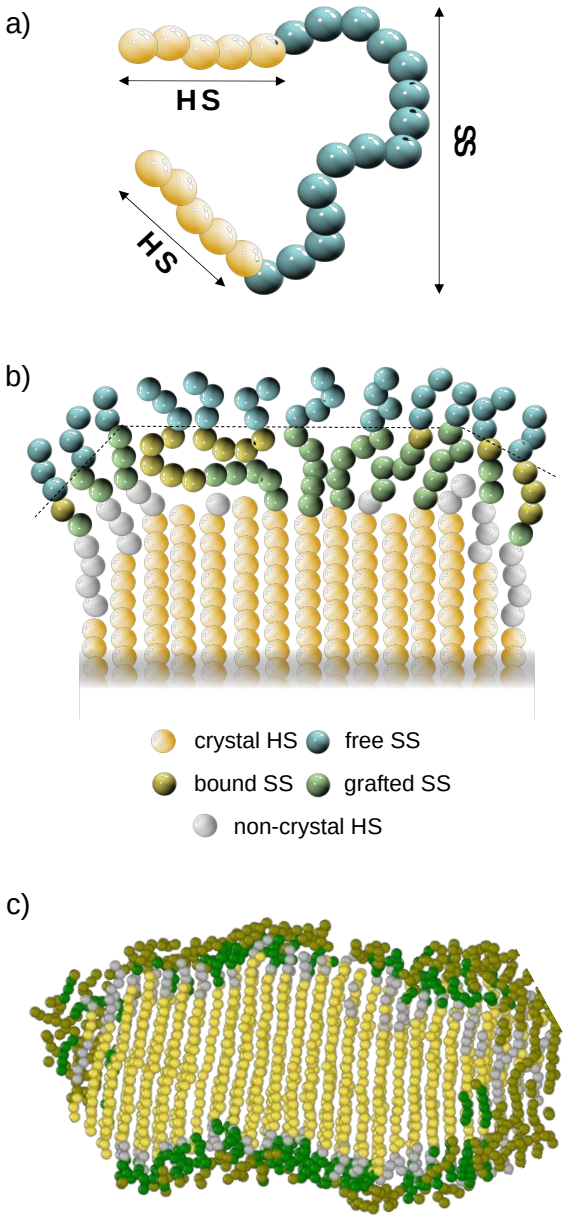

Figure 3: a) Schematic representation of a simulated triblock copolymer that would correspond to *HS*5. b) Different types of HS and SS beads present in the simulation boxes. The dashed line

represents the distance 4 σ_u from the interface. c) Sectional view of a crystallite obtained in the HS20 system by molecular dynamics. The color code is the same as in b) and the free-SS beads are not represented. The discrimination between the various types of SS beads is at the heart of the calculation of the amorphous phase hardening. No chain bending is observed.

TABLE I. Architecture of MBCs, variables are defined in the text. Chains are generated at $T = 4\ \varepsilon_u/k_B$ (molten state) with the constraint to satisfy $N/N_e = 4.8$. The antepenultimate and the penultimate columns are the volume fraction of HS crystallites (Φ) and the percentage of HS beads that effectively crystallize at $T = 1.5\ \varepsilon_u/k_B$ (ξ_{HS}). We also give respectively the mean square end to end distance of the neat SS and neat HS at $T = 4\ \varepsilon_u/k_B$, $< R_{SS}^2 >= 1103.8\ \sigma_u^2$ and $< R_{HS}^2 >= 1237.8\ \sigma_u^2$, and the number of beads per entanglement of the neat SS at $T = 1.5\ \varepsilon_u/k_B$, $N_e^{SS} = 20.9$.

System	N_{HS}[1] -	N_{SS}[2] -	N[3] -	x_{HS}[4] %	N_e[5] -	N/N_e -	Φ[6] vol.%	ξ_{HS}[7] %	*Percolation* -
Neat SS	0	212	212	0.0	44.0	4.8	0.0	0.0	*No*
HS6	6	194	206	5.8	42.7	4.8	0.0	0.0	*No*
HS8	8	188	204	7.8	42.3	4.8	1.1	14.3	*No*
HS9	9	185	203	8.9	42.1	4.8	3.1	35.1	*Bound*
HS10	10	182	202	9.9	41.8	4.8	4.2	42.0	*Bound*
HS11	11	179	201	10.9	41.6	4.8	4.7	43.3	*Bound*
HS12	12	176	200	12.0	41.4	4.8	5.5	46.1	*Bound*
HS13	13	172	198	13.1	41.1	4.8	6.7	50.8	*Bound*
HS14	14	169	197	14.2	40.9	4.8	7.6	53.5	*Bound*
HS15	15	166	196	15.3	40.7	4.8	8.7	57.0	*Bound*
HS17	17	160	194	17.5	40.8	4.8	10.9	62.4	*Bound*
HS20	20	150	190	21.1	39.4	4.8	14.3	67.8	*Grafted*

Neat HS	100	0	100	100	23.2	4.3	61.4	61.4	-

1. Number of beads in (monodisperse) HS
2. Number of beads in (monodisperse) SS
3. Number of beads per chain
4. Mass fraction of HS beads in the simulation box (soft- and hard-beads have a different mass)
5. Average number of beads between entanglements (Kroger)
6. Volume fraction in HS crystallites determined from the number of beads belonging to crystallites. Amorphous and crystalline phases densities are not significantly different in the simulations (both are around 0.30 ± 0.01 beads per unit volume).
7. Fraction of crystallized HSs
8. Detection of percolation. *No* : no percolation. *Bound* : Percolation occurs in at least two directions by considering crystallites, grafted-SS, and bound-SS. *Grafted* : Percolation occurs in at least two directions by considering crystallites and grafted-SS only (See Section 3.2).

All simulations are performed in the NPT ensemble with Nosé-Hoover thermostat and barostat, using periodic boundary conditions. Newton's equations of motion are integrated with the velocity Verlet method with the time step $\Delta t = 0.0025\ \tau_u$. Pressure is fixed at $P = 0.5\ \varepsilon_u/\sigma_u^3$. All molten copolymers are relaxed at $T = 4\ \varepsilon_u/k_B$ for $2 \times 10^5\ \tau_u$ and are subsequently cooled down to $T = 1.5\ \varepsilon_u/k_B$ at a cooling rate of $5 \times 10^{-6}\ \varepsilon_u/k_B/\tau_u$ and relaxed again at this temperature for $7.5 \times 10^5\ \tau_u$ ensuring strong and negligible crystallization of HS and SS respectively. $T = 1.5\ \varepsilon_u/k_B$, is slightly above the glass transition temperature of HS, close to $T = 1.4\ \varepsilon_u/k_B$, and well above that of SS, close to $T = 0.46\ \varepsilon_u/k_B$. No independent amorphous HS domain is observed at this temperature. All simulations are performed in three dimensions using the open-source code LAMMPS[32] and images are generated with OVITO[33]. All triblock copolymers are seen to crystallize except HS6 that remains fully amorphous. The fraction and morphology of the crystalline phase are extracted with a hierarchical clustering method[26], explained in detail in Supplementary Information (SI Section 1). A direct comparison of $\Phi = f(x_{HS})$ with experimental data from twelve different multiblock systems is also provided in SI Section 1 to evidence the relevancy of our simulations. Importantly, HS-folding was never observed (whatever the HS

length) as emphasized Figure 3c. This confirms that our triblock copolymers can be seen as supramolecular polymers in the sense that a given sticker cannot associate with itself, which further ensures that crystallites connect N_{ce} distinct elastically active strands, as hypothesized in the topological model (see e.g., Eq.3 and Figure 2).

To rationalize the reinforcement at high Φ involving the hardening of the soft phase, different categories of beads are defined according to their type and environment: crystalline HSs, non-crystalline HSs, crystalline SSs and non-crystalline SSs (see Figure 3b-c). The latter includes three sub-ensembles. (i) "*Grafted*" SS beads are the ones whose chemical distance from a bead belonging to a crystalline-HS is not further than five covalent bonds. (ii) "*Bound*" SS beads are located at a spatial distance shorter than 4.0 σ_u from any crystalline-HS bead, excluding "*grafted*" beads. (iii) "Free" SS beads include all other non-crystalline SS beads located further from the interface with the HS crystallites.

Note that because in our simulations the extreme majority (if not all) of the HSs are gathered into crystallites, the fraction of non-crystalline HS beads does not impact the value of N_{ce}, nor, consequently, the topological reinforcement (Eq. 6 and Section 3.1). In addition, although they certainly participate to the mechanical response of the materials because of their sluggish dynamics, they cannot bridge crystallites alone because of covalently connected SS. In other words, they never "percolate" making them irrelevant in our Eq. 11 in which H quantifies the hardening of the softest type of percolating beads (See Section 3.2). For these two reasons, non-crystalline HS beads are not considered in the following.

3. Results and Discussion

3.1. Topological considerations.

Figure 4 shows the relaxation shear modulus as a function of time $G(t)$ computed using the Green-Kubo method (GK)[34] and averaged over the three principal directions for various HS contents such as

$$G(t) = \frac{V}{k_B T} \langle \sigma_{\alpha\beta}(t) \sigma_{\alpha\beta}(0) \rangle_{\alpha \neq \beta} \tag{14}$$

where V si the simulation box volume, k_B is the Boltzmann's constant and $\sigma_{\alpha\beta}$ represents the $\alpha\beta$ (shear) stress component of the stress tensor $\bar{\bar{\sigma}}$.

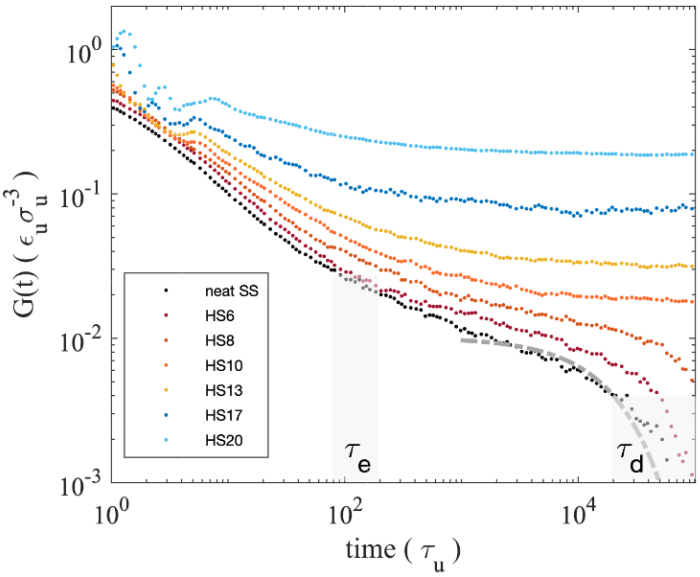

Figure 4: Relaxation shear modulus of MBC with growing content in HS. The dashed-dotted green line is a fit to the neat SS data based on Eq. 17. Some data are not displayed for clarity, the whole data set is reported in SI section 2.

At short time, the modulus appears to be almost independent of the MBC composition because it is dominated by the fast relaxation modes of the SSs. However, at time longer than the entanglement time τ_e, i.e., the Rouse relaxation time of an entanglement strand, the growing content of HS within the chain results in a strong reinforcement manifested by large plateau

values. According to the GK calculations, the neat soft matrix (denoted neat-SS) exhibit $\tau_e \approx 10^2\ \tau_u$, corresponding to the beginning of its rubbery plateau. This result is in good agreement with the Rouse scaling law $\tau_e = \tau_k N_{k,e}^2 = 157\ \tau_u$ with $\tau_k = 15\ \tau_u$ being the Kuhn segment relaxation time and $N_{k,e} = \frac{N_e}{C_\infty} = 3.2$, where $C_\infty = 6.53$ represents the number of beads per Kuhn segment. Note that τ_k can be estimated from our simulations by calculating first $MSD(\tau_k) =< 2R_g^2(C_\infty) >$, corresponding to ca. 5 σ_u^2 (see Figure 6f), and reporting the value on the $MSD = f(\tau)$ plot (see Figure 6f). Alternatively, one can approximate $< 2R_g^2(C_\infty) > \approx l_k^2$, where $l_k = 2.42\ \sigma_u$ is the SS Kuhn length (see Section 3.2).

On the other hand, the end of the plateau is assigned to the terminal relaxation time τ_d, close to $10^4\ \tau_u$ in Figure 3. This value, albeit lower, is in fair agreement with the reptation scaling law given by $\tau_d = \frac{\tau_k N_k^3}{N_{k,e}} = 1.6\ 10^5\ \tau_u$, where N_k is the number of Kuhn segments per chain. As expected, the decay of the modulus at $t > \tau_d$ is not visible in strongly associated systems where the chains diffusion is suppressed. In between these two limits, one can see that $G(t)$ of the neat soft polymer does not exhibit a true plateau but rather a slowly decreasing profile, as it is mostly observed experimentally in polymer melts because of contour length fluctuation and constraint release effects[35]. In order to extract a plateau modulus value for each HS content, we fit the $G(t)$ curves with a decreasing exponential function above $10^3\ \tau_u$ (see the dash-dot grey line in Figure 4) as follows

$$G(t > 10^3\ \tau_u) = G_N^{MBC} e^{-t/\tau} \qquad (15)$$

Beyond the satisfying qualitative trend of the mechanical properties showing both the expected gelation and reinforcement effects, we focus on the quantitative aspect of the latter parameter in Figure 5. Here, CGMD results (hollow blue squares) are confronted to former experimental data measured from different MBCs[23] (black symbols) emphasizing a good agreement between

physical and numerical experiments, further evidenced by exponential fits ($\chi = e^{A\Phi}$) providing similar parameters: A =18.38 and 19.57, respectively. This remarkable agreement, spanning the whole Φ range, suggests therefore that a meticulous analysis of the structure of simulated systems (accessible in a straightforward way) is likely to provide decisive information about the origin of the reinforcement, allowing therefore to challenge our mechanistic model, i.e., our fundamental understanding of the reinforcement. Following this logic, we fed Eq. 6 with the average value of N_{ce} directly accessible from the simulated systems to calculate their "theoretical reinforcement". These predictions are displayed in Figure 5 as red circles. Strikingly, restricting the comparison to $\Phi < 8\ vol.\%$ shows that beyond the success of our approach to rationalize the reinforcement from DSC (Φ) and SAXS (d^*) experiments (see refs. [21,23]), our model is also able to predict satisfyingly the reinforcement observed in simulation boxes based on their structure. This important result supports therefore the prominent role of the N_{ce} parameter in the mechanism of reinforcement enabling to progress on the understanding of the physics of relatively loose ($\Phi < 7-8\ vol.\%$) associative polymers (here represented by a loose network of crystallites).

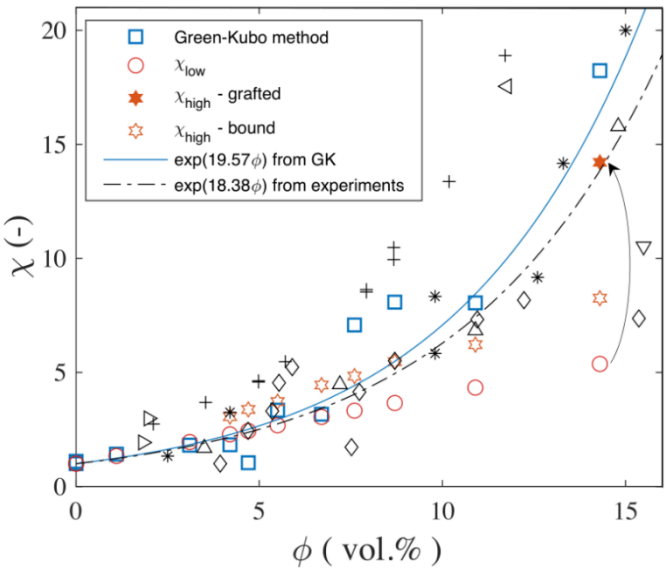

Figure 5: Reinforcement as a function of the HS crystallites volume fraction in simulated MBCs. Blue squares represent the GK calculations. Red circles are calculated from the mechanistic

model (Eq. 6) applied on the simulation boxes. Orange hollow and full stars are calculated from Eq. 11 where the hardening parameter H is estimated in Section 3.2 assuming the percolation of *grafted*- plus *bound*-SS and sole *grafted*-SS respectively. The blue solid and the black dashed lines are respectively exponential fits of GK simulated data and experimental data, reproduced from [21]. The arrow emphasizes the effect of SS dynamical slowdown on the reinforcement in HS20. Black data correspond to experimental measurements performed on various MBCs from the literature: ◇ [36], △ [21,24,25], ∇ [37], + [38], ◁ [39], ∗ [40] and ▷ [41].

While topological links dominate the plateau modulus of MBCs at low Φ, the situation is expected to become more intricate upon increasing the crystallites content. In particular, because the average distance between crystallites' walls (d_w) becomes smaller than the average equilibrium end-to-end distance of neat SS ($< R_{SS}^2(n) >_0^{\frac{1}{2}}$) (see Figure 6a for simulated MBCs), the latter's average conformation must be significantly impacted. Our simulations enable to illustrate this effect by plotting the SS elongation ratio of MBCs with respect to the neat soft matrix ($\lambda = < R_{SS}^2(n) >_{\Phi}^{\frac{1}{2}} / < R_{SS}^2(n) >_0^{\frac{1}{2}}$) and by observing its deviation from unity as presented in Figure 6b. This representation first reveals in all the systems a growing value of λ at low n indicating that the SSs in immediate vicinity to the crystallites exhibit some degree of stretching (up to ≈30 % in HS20). In addition, the maximum value of λ appears to grow with the size of the HSs (and Φ, see Table 1), being reminiscent of the Alexander-de Gennes brush theory[10]. In brief, the larger the crystallites, the higher the number of SS connected to them, and the higher the average degree of stretching of the SS due to entropic considerations (as evoked in[21]). This observation from CGMD simulation, further confirms experimental results on MBCs indicating that the section (or width) of the crystallites are expected to grow with the length of the HS (enhancing also Φ)[25]. For higher values of n, a pronounced decrease of λ is observed; it can be

interpreted as the end of the brush allowing the chain to adopt a conformation closer from a Gaussian coil, albeit non-fully equilibrated. Finally, λ is almost always observed to re-increase at high n indicating the presence of another SS brush configuration coming from the crystallization of the HS at the other chain extremity. The important message is therefore that the SS beads close to the crystallites are very likely to belong to stretched polymer segments that can be elongated up to a factor 1.2-1.3 with respect to the neat SS coils and that this effect is accentuated with increasing the length (and the volume fraction) of HSs.

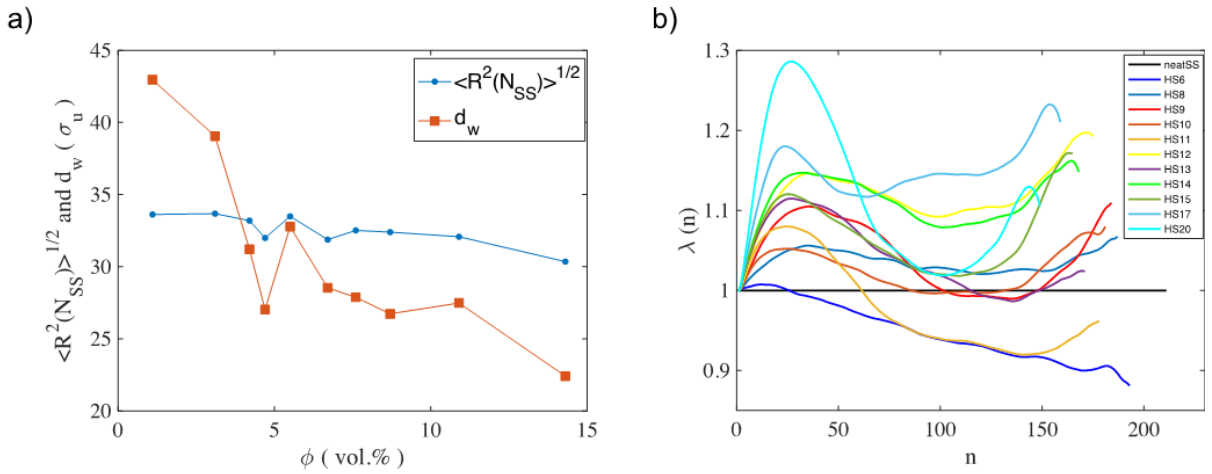

Figure 6: a) Average SSs end-to-end distance and distance between crystallites walls as a function of the volume fraction in crystallites. b) Elongation ratio of the SS for various HS length (corresponding to various volume fraction in crystallites).

Beyond the quantitative analysis of the chain conformation, their topology is also interesting to investigate since it can be related to the fraction of elastically active segments, being of possible interest to quantify the reinforcement. In particular, our simulations give us the possibility to discriminate the chain segments (accounting for both SS and HS beads) according to three types: "*loops*", "*ties*" or "*cilia*". *Loops* correspond to segments being connected at both ends to the same crystallites, *ties* are segments that bridge two distinct crystallites while *cilia* are connected to a single one. In addition, *Free chain* beads belong to fully amorphous chains. The result of this

analysis on the whole set of simulation boxes is presented in Figure 7 where the cumulative fraction of each type of segment is represented through a bar diagram.

A first observation is that under a critical size (HS6), the MBCs are not able to crystallize at $T = 1.5\ \varepsilon_u/k_B$, as one may have anticipated from the classic picture of block copolymers in which the degree of phase separation (and possible crystallization) strongly depends on the degree of segmentation[8,20]. Above this threshold, the HSs connectivity increases very quickly resulting in 50 % and 90 % of the beads (i.e., of the chains) being involved into associated structures for HS8 and HS9, respectively. Note however that a network spanning the whole material only appears from HS10 as evidenced in Figure 4 by the non-relaxing $G(t)$ curve at long time. Below this limit, one can thus evoke chains aggregate (or possibly rings) that have a finite relaxation time.

Then, following the fraction of beads involved into *cilia* segments provides a direct quantification of the number of triblock chains being connected only once. As expected, increasing the HS length (and thus the volume fraction in crystallites) is seen to dramatically reduce the *cilia* fraction, passing from more than 40 % in HS8 to only 10 % in HS14. Interestingly, while the fraction of *cilia* is less than 5 % in HS20, the HS crystallinity is 67.8 % (see Table 1), indicating unambiguously that the great majority of chains can be connected from a topological point of view with only 2/3 of the HS beads belonging to crystallites. A direct corollary of this observation is that the HSs do not crystallize on their whole length, as already evidenced experimentally in a number of publications[19,25], in spite of their monodisperse nature in our simulations.

Besides, the fraction of non-elastically active segments per chain can be estimated to $2N_e/N$ and $N_e/(N - N_{HS})$ for *free chains* and *cilia* respectively, representing 42 % $\pm$ 3 % and 22 % $\pm$ 2 % of the polymer regardless of the HS content. Then, because *loops* consist of monodisperse SSs satisfying systematically $N_{SS} \gg N_e$ (Table 1), we estimate that they are all fully elastically active similarly as *ties*. Based on Figure 7, the fraction of non-elastically active segments represents therefore 28 % in HS8 before to fall to 14 % in HS9 and 6 % in HS10. At higher HS content, the

material can be approximated as fully elastically active (while containing less than 5 vol.% in crystallites) in agreement with the assumptions of our analytical model (Eq. 4).

Finally, beyond the expected growth of both *ties* and *loops* fractions with increasing the HS content, it is worth to observe that tie molecules always dominate, representing up to 65 % of the material in HS14 and HS15, before a slight decrease in HS17 and HS20 where the relative fraction of *loops* is seen to progress a little, passing from ca. 16 % (HS15) to 22 % (HS20). We speculate that the latter evolution is related to the higher degree of phase separation occurring before the crystallization at higher HS content[27], promoting local crystallization that reduces the degree of SS stretching, in good agreement with Figure 6b (see e.g., the lower $\lambda(n = N_{SS})$ for HS20).

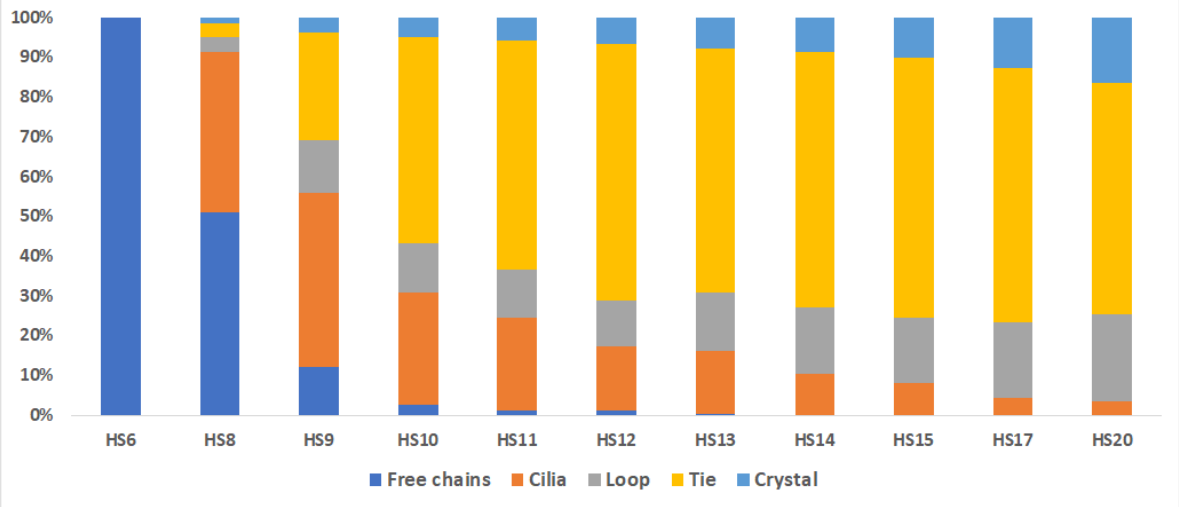

Figure 7: Relative populations of *free chains*, *cilia*, *loop*, *tie* and crystal segments at $T = 1.5\ \varepsilon_u/k_B$. The fractions are calculated based on the number of beads belonging to each type of segment (number density).

The key messages to draw from this first series of result is that CGMD simulations well reproduce the reinforcement trends observed experimentally from 0 to ca. 15 vol.% in crystallites. Remarkably, our analytical model based on the degree of connectivity reproduces

successfully both physical and numerical experiments from their own structural features (N_{ce}, Φ) that we extract either from SAXS and DSC[21], or numerical analysis. However, our topological picture fails above ca. $\Phi = 8\ vol.\%$, which is explained by an out-of-equilibrium conformation of the soft phase. The latter is evidenced by numerical simulations that emphasize non-Gaussian conformations. Finally, the fraction of non-elastically active segment is found not to exceed ca. 15 % (from HS9 and above), in fair agreement with the hypothesis of a fully elastically active soft phase as considered in our analytical model (above $\Phi \approx 3$ vol.%). In the next section, we shall investigate the dynamical behavior of the "perturbed" soft phase to rationalize the reinforcement at high Φ.

3.2. Dynamical considerations.

Together with conformational perturbations come dynamical ones. Many authors notably reported the slowdown of the adsorbed polymer layer in nanocomposites, often termed as "immobilized" or "interfacial" layer[42,43], including its effect on the (simulated) crystallization kinetics[44,45]. In our case, HS-based crystallites play the role of the rigid phase, being covalently connected to the matrix. In terms of mechanical properties, dynamical slowing down is equivalent to a hardening, possibly resulting in the formation of a hybrid percolated network made of hard fillers bridged by hardened (or "glassy") polymer segments[24,46,47]. In this case, the apparent reinforcement is expected to be far stronger than estimations relying on sole topological considerations. The results reported in Figure 5 follow this global trend, clearly indicating that, at high Φ, topological arguments become insufficient to rationalize the mechanical properties. In ref.[21], this mismatch was actually assigned to the SS hardening, and fitted on experimental data with Eq. 11 resulting in $H = 2.23$.

In the following, our idea relies on using the $G(t)$ curve of the neat SSs presented in Figure 5 to calculate independently the hardening of the soft phase within each MBC. In other words, we wonder what would be the $G(t)$ response of the sole soft phase encompassed within an MBC at a

given Φ. To do so, we first calculate the average mean square displacement (MSD) of each sub-ensemble of beads, namely *free*, *bound* and *grafted*-SSs, that we report in Figure 8a-c. For the sake of completeness, we also display in Figure 8d the MSD of HSs that exhibit a plateau at long time indicating their association (crystalline and amorphous HS beads have similar dynamics). Interestingly, sorting the beads according to these four groups emphasizes that the HS content does not significantly impact the dynamics of the beads, regardless of their type (whereas it does enhance the fraction of slower *bound* and *grafted* SS beads). This can be understood based on the local length scale criteria used to classify the beads, limiting cooperation effects. More interestingly, Figure 8e reveals however that strong dynamical differences exist between the different types of beads. In fact, while the upper line represents the dynamics of neat soft polymers, it clearly appears that *free*, *bound* and *grafted*-SS are less and less mobile in this order. Associated HSs are of course even less mobile.

Translating this dynamical slowdown in terms of modulus would then result in a shift of the neat SSs $G(t)$ curve towards longer time, synonymous of a higher modulus at a given timescale. Applying this philosophy requires nevertheless several ingredients: (I) the appropriate time scale to calculate the hardening, (II) the quantification of the dynamical slowing down of each type of SS beads in presence of crystallites, and (III) the spatial distribution of each type of beads within the materials, allowing to track possible percolation effects.

Regarding the relevant time scale (I), one needs to keep in mind that the reinforcement is defined from the rubbery plateau of the neat SSs, satisfying $\tau_e < t < \tau_d$, corresponding roughly to $10^2\ \tau_u < t < 10^4\ \tau_u$ in Figure 4. In fact, the $G(t)$ profile can be seen as a broken line where the plateau extremities correspond respectively to the entangled strand relaxation and chain diffusion while the plateau itself is assigned to chain motion at intermediate length scales[10]. Although the latter portion was originally modeled as a true plateau, refinements were made to better match experimental observations – indicating systematically a slight negative slope upon

increasing time. One could therefore wonder about the most pertinent time (from τ_e to τ_d) to read the "plateau" modulus value. Interestingly, Figure 7 shows strong deviations of the MSD when passing from the neat-SSs to SSs included in MBCs, right from the beginning of the plateau modulus at $t \approx 10^2\ \tau_u$. This observation confirms therefore that the association of HSs not only inhibits chains diffusion at long time, (τ_d) but also constrains the SS motion at a much shorter timescales (τ_e), being therefore relevant to investigate the hardening of the soft phase.

One then needs to focus on the dynamics of the different groups of SS beads (II), at the relevant time scale. Based on the above-mentioned arguments, the slowdown generated by the presence of the crystallites (δ) is calculated as

$$\delta_j^i = \frac{\tau_j^i(MSD_{SS}(\tau_e))}{\tau_e} \tag{16}$$

where the *i* superscript refers either to *free*, *bound* or *grafted* beads and the *j* subscript refers to the HS content. MSD_{SS} is the mean square displacement of the neat SSs, here determined at τ_e. We refer the reader to Figure 8f for the graphical representation of these parameters in HS20 and to Table 2 for the whole set of δ_j^i values that we determined at 100, 150 and 200 τ_u (corresponding to ca. 1, 1.5 and 2 τ_e) to highlight the weak dependence of these results around τ_e since we chose it as the relevant timescale.

Once the dynamical slowdown of the different groups of SS beads quantified, the next step consists of transposing this dynamical variation in terms of modulus. This is performed by using the neat-SS curve $G_{SS}(t)$ presented in Figure 4. Similarly as for the reference timescale, we choose $G_{SS}(\tau_e)$ as the reference modulus for the neat soft matrix. Then, the different values of the modulus corresponding to each type of SS beads and crystallites contents are determined from the dynamical slowdown as follows

$$G_j^i = G_{SS}(\tau_e/\delta_j^i) \tag{17}$$

that one can directly use to calculate the soft-phase hardening for the various types of SSs and MBC compositions as

$$H_j^i = \frac{G_j^i}{G_{SS}(\tau_e)} \ . \tag{18}$$

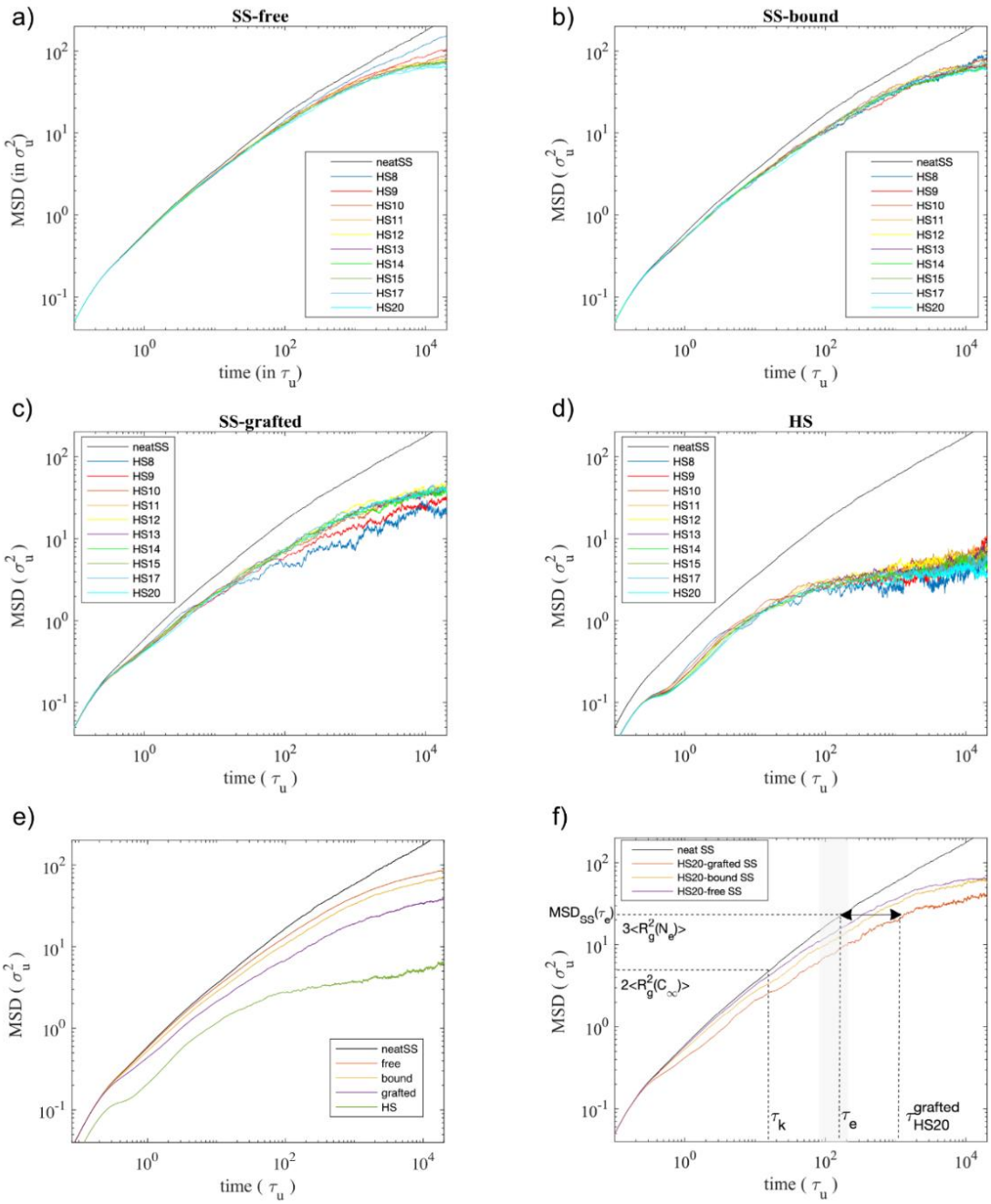

Figure 8: Mean square displacement as a function of time for the different types of beads: a) *Free*-SS, b) *Bound*-SS, c) *Grafted*-SS and d) HSs. For the sake of comparison, neat SS appears in black. e) Average MSD of each type of beads emphasizing dynamical heterogeneities in the MBC. f) Focus on the case of HS20. The double arrow represents the dynamical slowdown as defined in Eq. 16.

Table 2: Dynamical slow down δ_i^j extracted from simulations at $\tau = 100, 150\ and\ 200\ \tau_u$ for *free*, *bound*-, and *grafted*-SS, for all MBCs in which the percolation of *grafted* or *grafted+bound-SS* was detected (see SI).

τ / **System**	$100\tau_u$			$150\ \tau_u$			$200\ \tau_u$		
	free	*bound*	*grafted*	*free*	*bound*	*grafted*	*free*	*bound*	*grafted*
HS10	1.48	2.12	7.21	1.53	1.97	10.81	1.57	2.00	10.53
HS11	1.54	2.01	6.00	1.57	2.39	7.99	1.69	2.63	10.50
HS12	1.54	2.15	4.50	1.64	2.17	4.33	1.70	2.20	4.62
HS13	1.57	2.13	5.22	1.78	2.33	6.60	1.75	2.40	6.00
HS14	1.62	2.18	5.55	1.81	2.60	7.33	1.85	2.30	9.50
HS15	1.59	2.40	5.90	1.77	2.59	6.49	1.85	2.78	6.73
HS17	1.72	2.07	4.60	1.77	2.33	5.31	1.70	2.22	7.72
HS20	1.94	2.84	5.55	2.01	2.87	7.33	1.85	2.68	7.54

Remarkably, the H values obtained for *grafted*-SSs, i.e., the most constrained SS beads, vary from 2.02 to 3.19 according to the MBC composition, reminding the value determined from fitting the experimental reinforcement with Eq. 11 in reference[21], providing $H = 2.23$ (assuming

a homogeneous hardening of the SSs). This result seems thus to support quantitatively our analytical model at high Φ, indicating that a hardening of the soft phase around 2 is enough to "fill the gap" (see the arrow in Figure 5) observed between experimental and numerical experiments on one side, and our purely topological approach (Eq. 5) on the other side. The transition from H to the reinforcement determination through Eq. 11 further requires to extract the values of the tube diameter a and the cell parameter u from the simulations. First, the tube diameter of the neat-SS system is evaluated through $a = l_k\sqrt{N_e^{SS}}$ where $l_k = \sqrt{< R_{SS}^2 >/(N-1)}$ is the Kuhn length of the SSs. At $T = 1.5\ \varepsilon_u/k_B$, this results in $l_k = 2.42\ \sigma_u$ and $a = 11.09\ \sigma_u$. Second, crystalline HSs form a body-centered orthorhombic structure of cell parameters $u_1 = 1.97\ \sigma_u$ and $u_2 = 3.42\ \sigma_u$ [26] that we can combine to define a unique cell parameter representing the average distance between the nearest chains in the crystallites such as $u = \sqrt{\left(\frac{u_1}{2}\right)^2 + \left(\frac{u_2}{2}\right)^2} = 1.97\ \sigma_u$.

As evoked at the end of the Section 2.1, the rationalization of the reinforcement through Eq. 11 lies on the emergence of a percolated network made of crystallites bridged by sluggish SSs. This scenario notably explains why the topological approach well describes the reinforcement at low Φ only, and the need to consider the dynamical slowdown of the soft phase at higher Φ. To verify this structural hypothesis, we studied the spatial distribution of each sub-ensemble of SS beads for the whole set of MBC compositions (ingredient III), paying a particular attention to the possible percolation of hybrid networks (see SI Section 3 for details on the percolation detection). Part of this analysis is presented in Figure 9a confirming the presence of well-isolated islands made of crystalline HSs surrounded by both *grafted*- and *bound*-SS at low Φ (in HS9) while a percolated network built from these core-shell objects emerges from $\Phi \approx 10\ vol.\%$, as presented in Figure 9b for HS17. Besides, the percolation threshold jumps to ca. $\Phi = 14.3\ vol.\%$

when the sole *grafted*-SS are considered, indicating that the "hardest hybrid network", made of HS crystallites bridged by *grafted*-SS, only exist in HS20 (Figure 9c). These two situations have been formalized in terms of mechanical reinforcement in Figure 5 where we provide predictions calculated from Eq. 11 according to the softest type of SS likely to percolate in each MBC. While hollow stars represent the reinforcement calculated from H^j_{bound}, i.e., in presence of a network percolating through both *grafted*- and *bound*-SS, the prediction represented by a full star (HS20) consider $H^j_{grafted}$, i.e., a higher degree of soft-phase hardening. (Note that although *free*-SS beads are slightly delayed with respect to the neat-SS dynamics, the corresponding H^j_{free}were too close to 1 to justify the calculation of a relevant MBC reinforcement in the case of "non-percolated MBCs" such as HS8 and HS9. This explains the two missing stars on the left-hand side of Figure 5).

These results illustrate the fact that the hardening of the soft phase growingly impacts the reinforcement of the MBC as a function of Φ and offers a quantitative estimation of this effect. They reveal that a significant (albeit modest) dynamical hardening is likely to start from 4.2 vol.% in crystallites (HS10), where the "dynamical" Eq. 11 provides a slightly higher reinforcement than the purely "topological" Eq. 5. Then, increasing progressively the crystallites content up to 10.2 $vol.\%$ (HS17) is seen to accentuate constantly the difference between these predictions, enabling to estimate the growing weight of the dynamical reinforcement within the global response of the material. Finally, at 14.2 $vol.\%$, the divergence of the reinforcement is understood as the percolation of the slowest (*grafted-SS*) beads, making the topology-originated reinforcement accounting for only 1/3 of the total material response.

As a final remark, we wish to remind the reader that in the case of HS20, a SS dynamical slow-down of $\delta^{grafted}_{HS20} = 5 - 8$ (see Table 2) was observed to increase the modulus by a factor 3 with respect to the pure topological reinforcement (see Figure 5). While in this article we assigned this

extra-hardening to the sole dynamical slowing-down of grafted-SS, other authors have suggested that the static conformational changes in the immediate vicinity of the hard-domains might contribute significantly (or predominantly) to this effect[48–50]. Interestingly, they notably evoke a restriction of the soft-phase bending ability likely to enhance the modulus, that one can imagine being particularly relevant in presence of a "hybrid percolated network". They however do not quantify directly the impact of the presence of brushes on the macroscopic modulus of their phase-separated telechelic polymers, that they describe through the interfacial layer model (ILM)[48, 49] or the percolation model[50] in which molecular description is not provided (the modulus of the interfacial layer is either taken as 1 GPa[48] or 100 MPa[49, 50] to match the experimental data). Although the present article supports the presence of the brush effect and partially quantifies it (Figure 6b), it must face a similar difficulty. In fact, it does not discriminate the role of the static conformation (that is ignored at the local lengthscale) from the dynamical slowing-down on the macroscopic modulus, which represents therefore a challenge for future investigations.

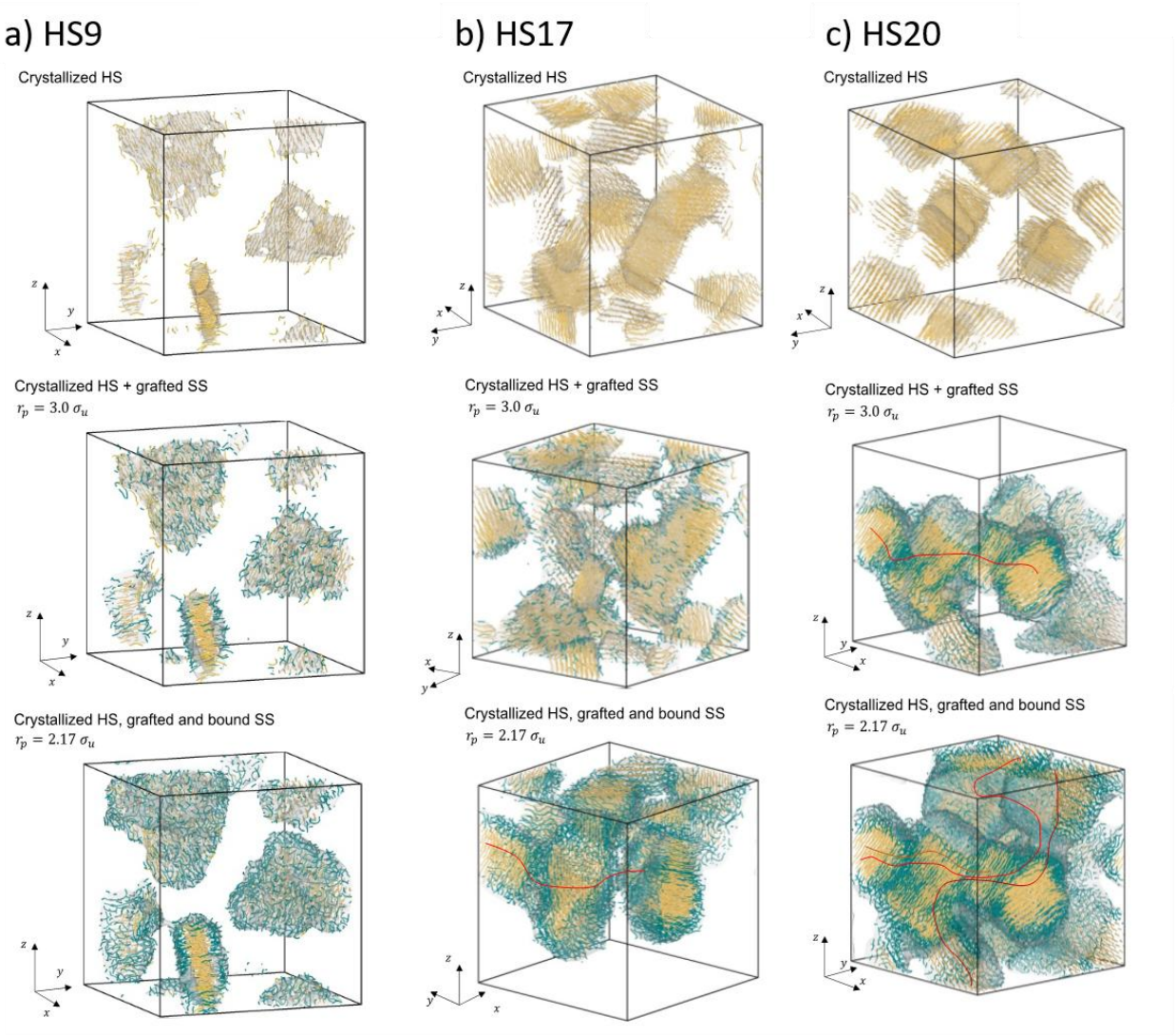

Figure 9: Graphical representation of the simulation boxes obtained for a) HS9, b) HS17 and c) HS20. The top row makes appear only crystallized HSs revealing no percolation. The middle row displays crystallized HS and *grafted*-SS beads revealing percolation along one axis in HS20 whereas no percolation in HS17. The bottom row displays crystalline HSs as well as *grafted*- and *bound*-SS indicating percolation in both HS17 and HS20 while no percolation is detected in HS9. Red solid lines highlight the percolated paths. Islands made of central crystallites and

surrounding SSs, being *grafted* and/or *bound*, are connected only if they are separated by a distance lower than r_p.

4. Conclusions

In conclusion, by combining experiments, simulations and an analytical description, we have provided a unifying picture of the microscopic origin of the reinforcement caused by the crystallization of hard-segments in multiblock copolymers. We believe that our approach is generic and relevant to describe the aggregation of associative groups in a broader class of supramolecular polymers. Moreover, while our work is restricted to the case of low and intermediate volume fractions in supramolecular aggregates ($0 < \Phi < 15\ vol.\%$), we believe that a similar approach could bring new insights on the reinforcement of denser systems ($15 < \Phi < 30\ vol.\%$) as long as their structure does not become too complex. In fact, the rationalization of semi-crystalline polymer containing "well-packed" spherulites and characterized by $\Phi \gg 30\ vol.\%$ appears more difficult, to address because of (i) the mechanical percolation of a complex crystallites network, and (ii) the absence of "free-SS" or "soft-matrix" serving as a reference in our work.

Of a particular interest, the degree of connectivity of the matrix, denoted N_{ce} (Eq. 3) in the text, has been identified both in physical and numerical experiments as a key topological parameter driving the reinforcement at low Φ. While we determined it through SAXS and DSC in the case of physical experiments[21], CGMD simulations makes it here straightforward to calculate. Beyond topological aspects, the use of CGMD makes it here possible to probe the dynamical slowing down of the soft phase in presence of crystallites, well-known to play a major impact on the modulus of semi-crystalline polymers and nanocomposites.

An important perspective of these simulations regards the rationalization of the mechanical behavior of crystallizable tri- (and possibly multi-) block copolymers under intermediate and large deformations. A first challenge resides in following the decrease of N_{ce} upon uniaxial stretching slightly above the linear regime to connect the number of HS-pull out events to the loss of modulus observed at the MBCs yield point[51–54]. More ambitiously, it would also be of great interest to monitor both the fraction and the dynamical behavior of each type of SS beads for several discrete values of large strain after having reached the equilibrium. These information would notably help to clarify the origin of the strain hardening beyond static chain stretching considerations. Lastly, isolating the role of the (static) brush effect caused by the aggregation of supramolecular moieties on the macroscopic modulus seems to be indispensable to reach a full understanding of the structure-properties relationship.

Author Information

Corresponding authors:

Julien Morthomas, julien.morthomas@insa-lyon.fr - 0000-0002-2513-5572

Guilhem P. Baeza, guilhem.baeza@insa-lyon.fr - 0000-0002-5142-9670

The authors declare no competing financial interest.

Figure 1a: Reprinted with permission from Ghiassinejad, S.; Mortensen, K.; Rostamitabar, M.; Malineni, J.; Fustin, C.-A.; van Ruymbeke, E. Dynamics and Structure of Metallo-Supramolecular Polymers Based on Short Telechelic Precursors. *Macromolecules* **2021**, *54* (13), 6400−6416. Copyright (2021) American Chemical Society.

Figure 2a: Reprinted with permission from Baeza, G. P. The Reinforcement Effect in Well-Defined Segmented Copolymers: Counting the Topological Constraints at the Mesoscopic Scale. *Macromolecules* **2018**, *51* (5), 1957−1966. Copyright (2018) American Chemical Society.

Acknowledgements

The authors acknowledge the computing time granted on the supercomputer Mogon at J. Gutenberg University of Mainz. Simulations were also performed on the massively parallel computer P2CHPD of the Fédération Lyonnaise de Modélisation et Sciences Numériques. M.N. thanks the french ministry of higher studies and research for his Ph.D. grant and Prof. Peter Virnau for his invitation to Mainz in 2020. J. M. thanks Junxiong Wang (INSA-Lyon) for technical support.

Supporting Information

1) Details on the hierarchical clustering method enabling crystallites detection.
2) Whole data set of Green-Kubo analyses
3) Details on the percolation detection.

References

(1) Zhang, Z.; Chen, Q.; Colby, R. H. Dynamics of Associative Polymers. *Soft Matter* **2018**, *14* (16), 2961–2977. https://doi.org/10.1039/C8SM00044A.

(2) Bentz, K. C.; Cohen, S. M. Supramolecular Metallopolymers: From Linear Materials to Infinite Networks. *Angew. Chem. Int. Ed.* **2018**, *57* (46), 14992–15001. https://doi.org/10.1002/anie.201806912.

(3) Yang, L.; Tan, X.; Wang, Z.; Zhang, X. Supramolecular Polymers: Historical Development, Preparation, Characterization, and Functions. *Chem. Rev.* **2015**, *115* (15), 7196–7239. https://doi.org/10.1021/cr500633b.

(4) Voorhaar, L.; Hoogenboom, R. Supramolecular Polymer Networks: Hydrogels and Bulk Materials. *Chem. Soc. Rev.* **2016**, *45* (14), 4013–4031. https://doi.org/10.1039/C6CS00130K.

(5) *Supramolecular Polymer Networks and Gels*; Seiffert, S., Ed.; Advances in Polymer Science; Springer International Publishing: Cham, 2015; Vol. 268. https://doi.org/10.1007/978-3-319-15404-6.

(6) Cordier, P.; Tournilhac, F.; Soulié-Ziakovic, C.; Leibler, L. Self-Healing and Thermoreversible Rubber from Supramolecular Assembly. *Nature* **2008**, *451* (7181), 977–980. https://doi.org/10.1038/nature06669.

(7) Jiang, L.; Griffiths, P.; Balouet, J.; Faure, T.; Lyons, R.; Fustin, C.-A.; Baeza, G. P. Magneto-Responsive Nanocomposites with a Metal–Ligand Supramolecular Matrix. *Macromolecules* **2022**, *55* (10), 3936–3947. https://doi.org/10.1021/acs.macromol.2c00256.

(8) Zhang, Z.; Liu, C.; Cao, X.; Gao, L.; Chen, Q. Linear Viscoelastic and Dielectric Properties of Strongly Hydrogen-Bonded Polymers near the Sol–Gel Transition. *Macromolecules* **2016**, *49* (23), 9192–9202. https://doi.org/10.1021/acs.macromol.6b02017.

(9) Leibler, L.; Rubinstein, M.; Colby, R. H. Dynamics of Reversible Networks. *Macromolecules* **1991**, *24* (16), 4701–4707. https://doi.org/10.1021/ma00016a034.

(10) Rubinstein, M.; Colby, R. H.; others. *Polymer Physics*; Oxford university press New York, 2003; Vol. 23.

(11) Ghiassinejad, S.; Mortensen, K.; Rostamitabar, M.; Malineni, J.; Fustin, C.-A.; van Ruymbeke, E. Dynamics and Structure of Metallo-Supramolecular Polymers Based on Short Telechelic Precursors. *Macromolecules* **2021**, *54* (13), 6400–6416. https://doi.org/10.1021/acs.macromol.1c00373.

(12) Sing, M. K.; Ramírez, J.; Olsen, B. D. Mechanical Response of Transient Telechelic Networks with Many-Part Stickers. *The Journal of Chemical Physics* **2017**, *147* (19), 194902. https://doi.org/10.1063/1.4993649.

(13) Mahmad Rasid, I.; Do, C.; Holten-Andersen, N.; Olsen, B. D. Effect of Sticker Clustering on the Dynamics of Associative Networks. *Soft Matter* **2021**, *17* (39), 8960–8972. https://doi.org/10.1039/D1SM00392E.

(14) Chen, Q.; Masser, H.; Shiau, H.-S.; Liang, S.; Runt, J.; Painter, P. C.; Colby, R. H. Linear Viscoelasticity and Fourier Transform Infrared Spectroscopy of Polyether–Ester–Sulfonate

Copolymer Ionomers. *Macromolecules* **2014**, *47* (11), 3635–3644. https://doi.org/10.1021/ma5008144.

(15) Jangizehi, A.; Ahmadi, M.; Seiffert, S. Emergence, Evidence, and Effect of Junction Clustering in Supramolecular Polymer Materials. *Mater. Adv.* **2021**, *2* (5), 1425–1453. https://doi.org/10.1039/D0MA00795A.

(16) Appel, W. P. J.; Portale, G.; Wisse, E.; Dankers, P. Y. W.; Meijer, E. W. Aggregation of Ureido-Pyrimidinone Supramolecular Thermoplastic Elastomers into Nanofibers: A Kinetic Analysis. *Macromolecules* **2011**, *44* (17), 6776–6784. https://doi.org/10.1021/ma201303s.

(17) Semenov, A. N.; Rubinstein, M. Dynamics of Entangled Associating Polymers with Large Aggregates. *Macromolecules* **2002**, *35* (12), 4821–4837. https://doi.org/10.1021/ma0117965.

(18) Annable, T.; Buscall, R.; Ettelaie, R.; Whittlestone, D. The Rheology of Solutions of Associating Polymers: Comparison of Experimental Behavior with Transient Network Theory. *Journal of Rheology* **1993**, *37* (4), 695–726. https://doi.org/10.1122/1.550391.

(19) Gaymans, R. J. Segmented Copolymers with Monodisperse Crystallizable Hard Segments: Novel Semi-Crystalline Materials. *Progress in Polymer Science* **2011**, *36* (6), 713–748. https://doi.org/10.1016/j.progpolymsci.2010.07.012.

(20) Baeza, G. P. Recent Advances on the Structure–Properties Relationship of Multiblock Copolymers. *Journal of Polymer Science* **2021**, *59* (21), 2405–2433. https://doi.org/10.1002/pol.20210406.

(21) Baeza, G. P. The Reinforcement Effect in Well-Defined Segmented Copolymers: Counting the Topological Constraints at the Mesoscopic Scale. *Macromolecules* **2018**, *51* (5), 1957–1966. https://doi.org/10.1021/acs.macromol.7b02208.

(22) Nébouy, M. Nanostructuration, Reinforcement in the Rubbery State and Flow Properties at High Shear Strain of Thermoplastic Elastomers: Experiments and Modeling, INSA de Lyon, Villeurbanne, 2020.

(23) Nébouy, M.; Louhichi, A.; Baeza, G. P. Volume Fraction and Width of Ribbon-like Crystallites Control the Rubbery Modulus of Segmented Block Copolymers. *J. Polym. Eng.* **2019**, *40* (9), 715–726. https://doi.org/10.1515/polyeng-2019-0222.

(24) Baeza, G. P.; Sharma, A.; Louhichi, A.; Imperiali, L.; Appel, W. P. J.; Fitié, C. F. C.; Lettinga, M. P.; Ruymbeke, E. V.; Vlassopoulos, D. Multiscale Organization of Thermoplastic Elastomers with Varying Content of Hard Segments. *Polymer* **2016**, *107*, 89–101. https://doi.org/10.1016/j.polymer.2016.11.010.

(25) Nébouy, M.; Almeida, A. de; Brottet, S.; Baeza, G. P. Process-Oriented Structure Tuning of PBT/PTHF Thermoplastic Elastomers. *Macromolecules* **2018**, *51* (16), 6291–6302. https://doi.org/10.1021/acs.macromol.8b01279.

(26) Morthomas, J.; Fusco, C.; Zhai, Z.; Lame, O.; Perez, M. Crystallization of Finite-Extensible Nonlinear Elastic Lennard-Jones Coarse-Grained Polymers. *Physical Review E* **2017**, *96* (5). https://doi.org/10.1103/PhysRevE.96.052502.

(27) Nébouy, M.; Morthomas, J.; Fusco, C.; Baeza, G. P.; Chazeau, L. Coarse-Grained Molecular Dynamics Modeling of Segmented Block Copolymers: Impact of the Chain

Architecture on Crystallization and Morphology. *Macromolecules* **2020**, *53* (10), 3847–3860. https://doi.org/10.1021/acs.macromol.9b02549.

(28) Zhai, Z.; Morthomas, J.; Fusco, C.; Perez, M.; Lame, O. Crystallization and Molecular Topology of Linear Semicrystalline Polymers: Simulation of Uni- and Bimodal Molecular Weight Distribution Systems. *Macromolecules* **2019**, *52* (11), 4196–4208.

(29) Zhai, Z.; Fusco, C.; Morthomas, J.; Perez, M.; Lame, O. Disentangling and Lamellar Thickening of Linear Polymers during Crystallization: Simulation of Bimodal and Unimodal Molecular Weight Distribution Systems. *ACS Nano* **2019**, *13* (10), 11310–11319. https://doi.org/10.1021/acsnano.9b04459.

(30) Mahaud, M.; Zengqiang, Z.; Perez, M.; Lame, O.; Fusco, C.; Chazeau, L.; Makke, A.; Marque, G.; Morthomas, J. Polymer Chain Generation for Coarse-Grained Models Using Radical-like Polymerization. *Communication in Computational Physics* **2018**, *24* (3), 885. https://doi.org/10.4208/cicp.OA-2017-0146.

(31) Kröger, M. Shortest Multiple Disconnected Path for the Analysis of Entanglements in Two- and Three-Dimensional Polymeric Systems. *Computer Physics Communications* **2005**, *168* (3), 209–232. https://doi.org/10.1016/j.cpc.2005.01.020.

(32) Plimpton, S. J. Fast Parallel Algorithms for Short-Range Molecular Dynamics. *Journal of Computational Physics* **1995**, *117* (1), 1–19.

(33) Stukowski, A. Visualization and Analysis of Atomistic Simulation Data with OVITO–the Open Visualization Tool. *Modelling and Simulation in Materials Science and Engineering* **2009**, *18* (1), 015012.

(34) Vladkov, M.; Barrat, J.-L. Linear and Nonlinear Viscoelasticity of a Model Unentangled Polymer Melt: Molecular Dynamics and Rouse Modes Analysis. *Macromolecular Theory and Simulations* **2006**, *15* (3), 252–262. https://doi.org/10.1002/mats.200500079.

(35) Cao, J.; Likhtman, A. E. Shear Banding in Molecular Dynamics of Polymer Melts. *Physical Review Letters* **2012**, *108* (2). https://doi.org/10.1103/PhysRevLett.108.028302.

(36) de Almeida, A.; Nébouy, M.; Baeza, G. P. Bimodal Crystallization Kinetics of PBT/PTHF Segmented Block Copolymers: Impact of the Chain Rigidity. *Macromolecules* **2019**, *52* (3), 1227–1240. https://doi.org/10.1021/acs.macromol.8b01689.

(37) Biemond, G. J. E.; Feijen, J.; Gaymans, R. J. Poly(Ether Amide) Segmented Block Copolymers with Adipic Acid Based Tetraamide Segments. *J. Appl. Polym. Sci.* **2007**, *105* (2), 951–963. https://doi.org/10.1002/app.26202.

(38) Krijgsman, J.; Husken, D.; Gaymans, R. J. Synthesis and Characterisation of Uniform Bisester Tetra-Amide Segments. *Polymer* **2003**, *44* (23), 7043–7053. https://doi.org/10.1016/S0032-3861(03)00681-5.

(39) Lee, H. S.; Park, H. D.; Cho, C. K. Domain and Segment Orientation Behavior of PBS-PTMG Segmented Block Copolymers. *J. Appl. Polym. Sci.* **2000**, *77* (3), 699–709. https://doi.org/10.1002/(SICI)1097-4628(20000718)77:3<699::AID-APP25>3.0.CO;2-H.

(40) van der Schuur, M.; Gaymans, R. J. Segmented Block Copolymers Based on Poly(Propylene Oxide) and Monodisperse Polyamide-6,T Segments. *J. Polym. Sci. A Polym.*

Chem. **2006**, *44* (16), 4769–4781. https://doi.org/10.1002/pola.21587.

(41) Versteegen, R. M.; Sijbesma, R. P.; Meijer, E. W. Synthesis and Characterization of Segmented Copoly(Ether Urea)s with Uniform Hard Segments. *Macromolecules* **2005**, *38* (8), 3176–3184. https://doi.org/10.1021/ma0478207.

(42) Papon, A.; Montes, H.; Hanafi, M.; Lequeux, F.; Guy, L.; Saalwächter, K. Glass-Transition Temperature Gradient in Nanocomposites: Evidence from Nuclear Magnetic Resonance and Differential Scanning Calorimetry. *Physical review letters* **2012**, *108* (6), 065702.

(43) Popov, I.; Carroll, B.; Bocharova, V.; Genix, A.-C.; Cheng, S.; Khamzin, A.; Kisliuk, A.; Sokolov, A. P. Strong Reduction in Amplitude of the Interfacial Segmental Dynamics in Polymer Nanocomposites. *Macromolecules* **2020**.

(44) Jabbarzadeh, A.; Chen, X. Surface Induced Crystallization of Polymeric Nano-Particles: Effect of Surface Roughness. *Faraday discussions* **2017**, *204*, 307–330.

(45) Jabbarzadeh, A.; Halfina, B. Unravelling the Effects of Size, Volume Fraction and Shape of Nanoparticle Additives on Crystallization of Nanocomposite Polymers. *Nanoscale Advances* **2019**, *1* (12), 4704–4721.

(46) Gong, S.; Chen, Q.; Moll, J. F.; Kumar, S. K.; Colby, R. H. Segmental Dynamics of Polymer Melts with Spherical Nanoparticles. *ACS Macro Letters* **2014**, *3* (8), 773–777. https://doi.org/10.1021/mz500252f.

(47) Fernández-de-Alba, C.; Jimenez, A. M.; Abbasi, M.; Kumar, S. K.; Saalwächter, K.; Baeza, G. P. On the Immobilized Polymer Fraction in Attractive Nanocomposites: Tg Gradient versus Interfacial Layer. *Macromolecules* **2021**, *54* (22), 10289–10299. https://doi.org/10.1021/acs.macromol.1c01135.

(48) Tress, M.; Ge, S.; Xing, K.; Cao, P.-F.; Saito, T.; Genix, A.-C.; Sokolov, A. P. Turning Rubber into a Glass: Mechanical Reinforcement by Microphase Separation. *ACS Macro Lett.* **2021**, *10* (2), 197–202. https://doi.org/10.1021/acsmacrolett.0c00778.

(49) Ge, S.; Samanta, S.; Tress, M.; Li, B.; Xing, K.; Dieudonné-George, P.; Genix, A.-C.; Cao, P.-F.; Dadmun, M.; Sokolov, A. P. Critical Role of the Interfacial Layer in Associating Polymers with Microphase Separation. *Macromolecules* **2021**, *54* (9), 4246–4256. https://doi.org/10.1021/acs.macromol.1c00275.

(50) Ge, S.; Samanta, S.; Li, B.; Carden, G. P.; Cao, P.-F.; Sokolov, A. P. Unravelling the Mechanism of Viscoelasticity in Polymers with Phase-Separated Dynamic Bonds. *ACS Nano* **2022**, *16* (3), 4746–4755. https://doi.org/10.1021/acsnano.2c00046.

(51) Sbrescia, S.; Ju, J.; Engels, T.; Van Ruymbeke, E.; Seitz, M. Morphological Origins of Temperature and Rate Dependent Mechanical Properties of Model Soft Thermoplastic Elastomers. *Journal of Polymer Science* **2021**, *59* (6), 477–493. https://doi.org/10.1002/pol.20200791.

(52) Deplace, F.; Wang, Z.; Lynd, N. A.; Hotta, A.; Rose, J. M.; Hustad, P. D.; Tian, J.; Ohtaki, H.; Coates, G. W.; Shimizu, F.; Hirokane, K.; Yamada, F.; Shin, Y.-W.; Rong, L.; Zhu, J.; Toki, S.; Hsiao, B. S.; Fredrickson, G. H.; Kramer, E. J. Processing-Structure-Mechanical Property Relationships of Semicrystalline Polyolefin-Based Block Copolymers. *Journal of Polymer*

Science Part B: Polymer Physics **2010**, *48* (13), 1428–1437. https://doi.org/10.1002/polb.21969.

(53) Niesten, M. C. E. J.; Gaymans, R. J. Tensile and Elastic Properties of Segmented Copolyetheresteramides with Uniform Aramid Units. *Polymer* **2001**, *42* (14), 6199–6207. https://doi.org/10.1016/S0032-3861(01)00088-X.

(54) Scetta, G.; Euchler, E.; Ju, J.; Selles, N.; Heuillet, P.; Ciccotti, M.; Creton, C. Self-Organization at the Crack Tip of Fatigue-Resistant Thermoplastic Polyurethane Elastomers. *Macromolecules* **2021**, *54* (18), 8726–8737. https://doi.org/10.1021/acs.macromol.1c00934.